Fragmentation dynamics of acetylene in collision with highly charged ions: Concerted and sequential breakage of CH and CC bonds

Yue Gao,[1,2] Yi Pan,[3] Shenyue Xu,[2,4,*] Kai-Chung Lau,[3,†] Hang Yuan,[1,2] Zhenyu Yan,[2,4] Dalong Guo,[2,4] Dongmei Zhao,[2] Xiaolong Zhu,[2,4] Shuncheng Yan,[2,4] Shaofeng Zhang,[2,4] Zhongfeng Xu,[1] and Xinwen Ma[2,4,‡]

[1]*MOE Key Laboratory for Nonequilibrium Synthesis and Modulation of Condensed Matter, School of Physics, Xi'an Jiaotong University, Xi'an 710049, China*

[2]*Institute of Modern Physics, Chinese Academy of Sciences, Lanzhou 730000, China*

[3]*Department of Chemistry, City University of Hong Kong, Tat Chee Avenue, Kowloon Tong, Hong Kong, China*

[4]*University of Chinese Academy of Sciences, Beijing 100049, China*

(Received 23 February 2022; accepted 22 December 2022; published 18 January 2023)

The three-body fragmentation of $C_2H_2^{3+}$ to $H^+ + C^+ + CH^+$ as a consequence of one CH and one CC bond breaking is investigated by 50-keV/u Ne^{8+} impact. All three fragments are detected in coincidence with a scattered projectile (either Ne^{7+} or Ne^{6+}) employing a reaction microscope, and their momentum vectors as well as the kinetic energies were obtained. Four distinguished structures are observed in the energy correlation spectra, indicating that abundant fragmentation mechanisms contribute to the $H^+ + C^+ + CH^+$ channel. The Newton diagrams and Dalitz plots are employed to trace fragmentation mechanisms. We found that both the concerted fragmentation and the sequential pathway with CH bond breaking prior to CC contribute to this channel. The possible electronic states of the $C_2H_2^{3+}$ precursor that may contribute to the identified fragmentation mechanisms are analyzed with the help of quantum chemical calculations. Furthermore, the influence of the collision dynamics between the projectile and the target to the dissociation mechanisms is discussed by comparing the contributions from the reaction channel with transferring one electron while ionizing the other two, i.e., T1I2, and the reversed channel T2I1. The T2I1 channel is observed to be more efficient to initiate fragmentation mechanisms leading to higher kinetic-energy release.

DOI: 10.1103/PhysRevA.107.012811

I. INTRODUCTION

The fragmentation mechanism of molecules is of fundamental interest in physics and chemistry, and has potential application in many research fields like evolution of interstellar media [1], radiation damage of living tissue [2], and plasma physics [3]. The three-body fragmentation of polyatomic molecules in which at least two chemical bonds break either simultaneously or sequentially has attracted great interest for several decades, and is still a hot topic in recent studies. Taking triatomic molecules as a prototype, many investigations have been performed to reveal details of the fragmentation mechanisms, such as the concerted and sequential breaking of chemical bonds, and the sequence of bond breaking in a sequential fragmentation process. In general, the three-body fragmentation of triatomic molecules including CO_2 [4–10], OCS [4,11–16], CS_2 [4,11,17,18], N_2O [4,19,20], NO_2 [11], and H_2O [21,22] has been well investigated.

Acetylene (C_2H_2) widely exists in nature, and plays a very important role in industry, e.g., oxyacetylene cutting and welding. As one of the smallest organic molecules, it has been chosen as a model system to investigate intramolecular proton migration and isomerization [23–30]. It was found that once the acetylene molecule is singly or doubly ionized, the acetylene-vinylidene isomerization can occur [23–28]. In the case of quadruply or higher ionization, the Coulomb explosion leads to complete fragmentation of the molecule into four separated nuclei [31–33]. The C_2H_2 molecule is of next higher degree of complexity than triatomic molecules for understanding three-body fragmentation mechanisms. Once three electrons are removed, the $C_2H_2^{3+}$ trication can dissociate into three products either through breakage of two CH bonds, i.e., the $H^+ + H^+ + C_2^+$ channel [33–36], or through breakage of one CH and one CC bond, i.e., the $H^+ + C^+ + CH^+$ channel. For the $H^+ + H^+ + C_2^+$ channel [35], we found in our previous study that the fragmentation mechanism exhibits characteristic features of fragmentation of linear triatomic molecules such as CO_2 [5]. The two CH bonds can break either simultaneously or sequentially. In addition, vibrational modes like molecular bending and asymmetric stretching also contribute significantly to the fragmentation. Nevertheless, in a later work by 3-keV/u Ar^{8+} impact [36], only concerted fragmentation is observed, demonstrating the sensitivity of fragmentation dynamics on the projectile energy [36].

In this paper, we focus on the three-body fragmentation channel

$$C_2H_2^{3+} \rightarrow H^+ + C^+ + CH^+. \quad (1)$$

This is the simplest system involving the breakage of both CH and CC bonds, and thus can serve as the prototype for

*s.xu@impcas.ac.cn
†kaichung@cityu.edu.hk
‡x.ma@impcas.ac.cn

understanding the competition between CH and CC cleavage in the decay of organic matter. In pump-probe measurements, this channel has been extensively selected as the probing channel to visualize intramolecular proton migration and isomerization occurring in $C_2H_2^+$ or $C_2H_2^{2+}$ [23,25,28]. Nevertheless, the fragmentation mechanism of $C_2H_2^{3+}$ trication to $H^+ + C^+ + CH^+$ has not yet been studied thoroughly, although this channel has been identified in several experiments [32–34]. In the present paper, the precursor $C_2H_2^{3+}$ is initiated by 50-keV/u Ne^{8+} impact. By measuring all three fragments in coincidence with the scattered projectile employing a reaction microscope, kinematically complete information is achieved. Detailed analysis of the momentum correlation between three fragments and their kinetic-energy (KE) distributions makes it possible to identify different mechanisms that contribute to this channel.

II. METHODS

A. Experimental details

The experiment was carried out by a reaction microscope (also called cold target recoil-ion-momentum spectroscopy) [37,38] connected to the 320-kV platform for multidisciplinary research with highly charged ions at the Institute of Modern Physics, Chinese Academy of Sciences. Since the details of the experimental setup have already described elsewhere [39], only a brief introduction is given here. The collimated 50-keV/u Ne^{8+} beam ($\approx$ 1-mm diameter) intersects with the gas jet formed by supersonic expansion of pure acetylene gas ($\approx$ 2-mm diameter). After collision, the ionic fragments from dissociation of C_2H_2 are extracted by a uniform electric field perpendicular to the directions of the beam and gas jet, and are detected by the time and position sensitive detector. The scattered projectile ions which capture one or more electrons from the target are separated from the residual Ne^{8+} beam by a parallel electrostatic deflector, and are detected by another time and position sensitive detector. The ionic fragments and the scattered projectile are stored in an event-by-event mode. During data analysis, the species of the ionic fragments are identified according to time-of-flight (TOF) information.

The precursor $C_2H_2^{3+}$ trications are produced through transfer ionization reactions:

$$\text{T1I2}: Ne^{8+} + C_2H_2 \rightarrow Ne^{7+} + C_2H_2^{3+} + 2e^-, \quad (2)$$

$$\text{T2I1}: Ne^{8+} + C_2H_2 \rightarrow Ne^{6+} + C_2H_2^{3+} + e^-. \quad (3)$$

Here T1I2 denotes that one of the target electrons is transferred to the projectile while another two electrons are ionized into the continuum, and so does T2I1. Unless otherwise specified, the data presented in this paper include the contribution from both reactions. The momentum vector of each fragment is calculated according to TOF and position information. Consequentially, the KE of each fragment, as well as the kinetic-energy release (KER, sum kinetic energy of the three fragments), are obtained.

The data are displayed in the Newton diagrams and the Dalitz plots to reveal momentum correlation between different fragments. In the Newton diagram [11], the momentum vector of H^+ is displayed as a unit on the horizontal axis, and the momentum vectors of C^+ and CH^+ are normalized and displayed in the upper and lower parts of the graph. The Dalitz plot was originally proposed for representation of τ-meson decay configurations [40]. In the past decade, it has been widely applied to represent the three-body breakup of molecules [5,35]. In the Dalitz diagram, X and Y coordinates are defined as

$$X = \frac{{P_2}^2 - {P_1}^2}{\sqrt{3}\Sigma {P_i}^2}, \quad (a)$$

$$Y = \frac{{P_3}^2}{\Sigma {P_i}^2} - \frac{1}{3}. \quad (b)$$

Here P_i $(i = 1, 2, 3)$ denotes the momentum of H^+, C^+, and CH^+, respectively.

B. Theoretical calculations

The state-average complete active space self-consistent-field (SA-CASSCF) method [41,42] with the cc-pVTZ basis sets is used to examine the energetics of ground and excited electronic states of $C_2H_2^{3+}$, and gain insight into the electronic states and mechanisms leading to $H^+ + C^+ + CH^+$ dissociation. In our calculations, the structures of $C_2H_2^{3+}$ trication were fully optimized at the SA-CASSCF/cc-pVTZ level. An active space (7, 10) with seven valence electrons distributed in ten molecular orbitals was used. For the excited-state calculations, the state averaging included the contributions of the ground state and 165 excited states (including 86 doublets, 64 quartets, and 15 sextets) of $C_2H_2^{3+}$ with energies up to 19 eV (Tables S1–S4 in the Supplemental Material [43]). The zero-point energy corrections at the SA-CASSCF/cc-pVTZ level, 0.30 eV for $C_2H_2^{3+}(^2\Pi_u)$ and 0.17 eV for $CH^+(^1\Sigma_g^+)$, were included. The MOLPRO2022 program suite [44] is used to perform all the calculations.

III. RESULTS AND DISCUSSION

A. Identification of fragmentation pathways

Figure 1(a) displays the correlation spectrum between KE of the proton and the sum KE of C^+ and CH^+. Four distinct islands marked as region I, II, III, and IV appear in this plot. The rich structures shown here indicate that different mechanisms may contribute to the $H^+ + C^+ + CH^+$ channel. Especially, the KE of the proton for region II is obviously higher than region I, while the sum energy of C^+ and CH^+ is almost the same for the two regions. This strongly indicates that the protons in I and II are emitted from different mechanisms. In Fig. 1(b) the data are presented in the correlation spectrum as a function of the KER and the sum KE of C^+ and CH^+. The KER values are different for different regions, indicating that different electronic states are involved.

Figures 2(a) and 2(b) represent the Newton diagram and Dalitz plot including all $H^+ + C^+ + CH^+$ events, respectively. The main spots locating in the forward and backward directions of the red arrow in Fig. 2(a) are attributed to the concerted fragmentation. Due to the linear geometry of C_2H_2, the three fragments produced in the concerted fragmentation process propagate mainly along the molecular axis. Also,

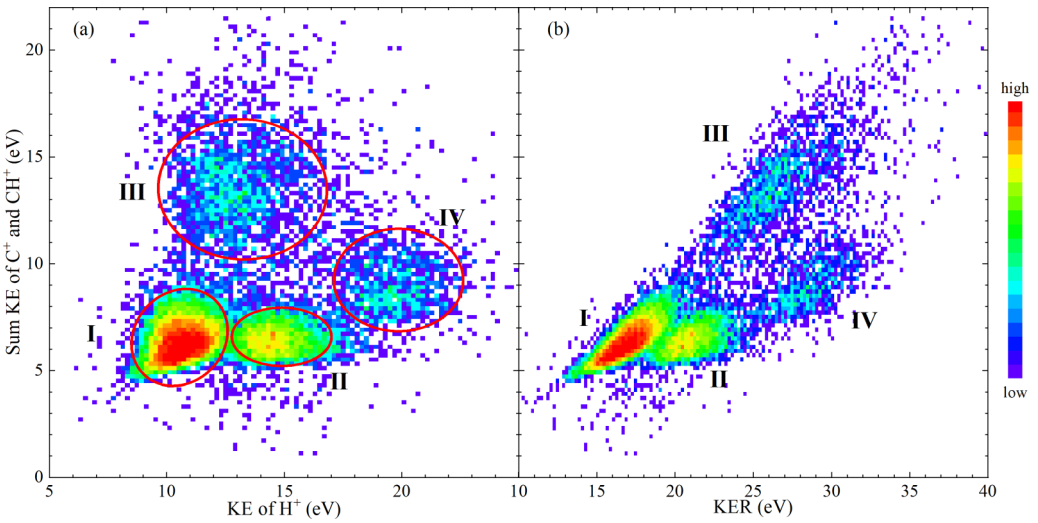

FIG. 1. Energy correlation spectra. (a) Sum KE of C^+ and CH^+ vs KE of H^+. (b) Sum KE of C^+ and CH^+ vs KER. Four isolated islands appear in both spectra. Events located in the different ovals marked I, II, III, and IV arise from different fragmentation mechanisms. I, concerted fragmentation of the low-lying states; II, sequential fragmentation; III, concerted fragmentation of the highly excited states; IV, sequential fragmentation of the highly excited states.

there is a semicircle structure labeled as black dashed semicircles which is a typical feature of the sequential fragmentation process [4]. Correspondingly, this semicircle structure is related to the strip along the orange dashed line in Fig. 2(b), which is the typical appearance of the sequential fragmentation in the Dalitz plot. In addition to the main spots and the semicircles, there are also additional distributions which cannot be well separated in Fig. 2(a). For example, in the upper plane of Fig. 2(a) there is a weak distribution in the right side of the main spot. To get an insight into the mechanisms behind all these structures shown in Figs. 2(a) and 2(b), we decompose the Newton diagram and the Dalitz plot by the filters of red ovals in Fig. 1(a), and show the partial plots in Figs. 2(c)–2(f) and 2(g)–2(j).

As shown in Figs. 2(c) and 2(g), the main spots for concerted fragmentation of the linear molecule are related to region I with the lowest KER, reflecting that this concerted process is probably from the low-lying electronic states of the $C_2H_2{}^{3+}$ trication. In addition, there are tail structures extending from the main spots. These tail structures show increased derivation of the C^+ (CH^+) momentum vectors from the direction (opposite direction) of the H^+ momentum. Such events are allocated to bending vibration that makes the acetylene molecule deviate from linear configuration. Figure 2(k) shows the KE distributions of the proton with different Dalitz filters shown in Fig. 2(g). The black solid rectangle covers mainly the main spot arising from concerted fragmentation of the molecules with linear configuration, while the red dashed rectangle covers mainly the tail structure following the main spot, which probably arises from molecular bending vibration. The difference in the KE curves illustrates that Coulomb potential experienced by the proton differs as the geometry changes due to bending vibration.

Region II corresponds to the semicircles in the Newton diagram and the strip in the Dalitz plot, as shown in Figs. 2(d) and 2(h). Such features demonstrate that region II arises from sequential fragmentation. The strip in Fig. 2(h) is parallel to the H^+ edge of the triangle. The distance from the data point to the H^+ edge is $P_{H^+}^2/\Sigma P_i^2$, i = 1, 2, 3. Thus the strip structure along the orange dashed line in Fig. 2(h) reflects that the momentum of the proton is independent of the other two fragments. Consequentially, the sequential process is assigned to the sequential pathway with H^+ emitted in the first step:

$$C_2H_2{}^{3+} \rightarrow H^+ + C_2H^{2+} \quad \text{step 1,} \tag{4a}$$

$$C_2H^{2+} \rightarrow C^+ + CH^+ \quad \text{step 2.} \tag{4b}$$

This is confirmed by plotting the KE distribution of the proton with different Dalitz filters. Figure 2(l) displays the proton KE distributions with different filters shown in Fig. 2(h). The curves for three filters are almost the same indicating that the KE of the proton is independent of the rotation of the intermediate dication. It can be seen in Fig. 2(d) that the intensity decreases gradually from one end of the semicircle to the other end. The uneven distribution is also observed in the Dalitz plot. It reveals that the lifetime of the intermediate C_2H^{2+} is shorter than its half-rotational period. This is different from sequential fragmentation of triatomic molecules like CO_2 [5] and OCS [15], but is consistent with sequential fragmentation of $C_2H_4{}^{3+}$ to $H^+ + H^+ + C_2H_2{}^+$ [45] and our observation for sequential fragmentation of $C_2H_2{}^{3+}$ to $H^+ + H^+ + C_2{}^+$ [35].

For region III the Dalitz plot in Fig. 2(i) exhibits a bright spot similar to the main spot in Fig. 2(g). In addition, the KE distributions of the proton shown in Fig. 2(m) vary as the Dalitz filter changes, indicating that the proton is emitted in correlation with the other two fragments. This is a typical feature of the concerted fragmentation process. The KER value for region III is about 9 eV higher than region I arising from low excited states. The events in region III are assigned to concerted fragmentation of the $C_2H_2{}^{3+}$ populated to higher electronic states. The spots in the Newton diagram of Fig. 2(e) are much broader than the main spots in Fig. 2(c). This can be qualitatively understood as the deformation of

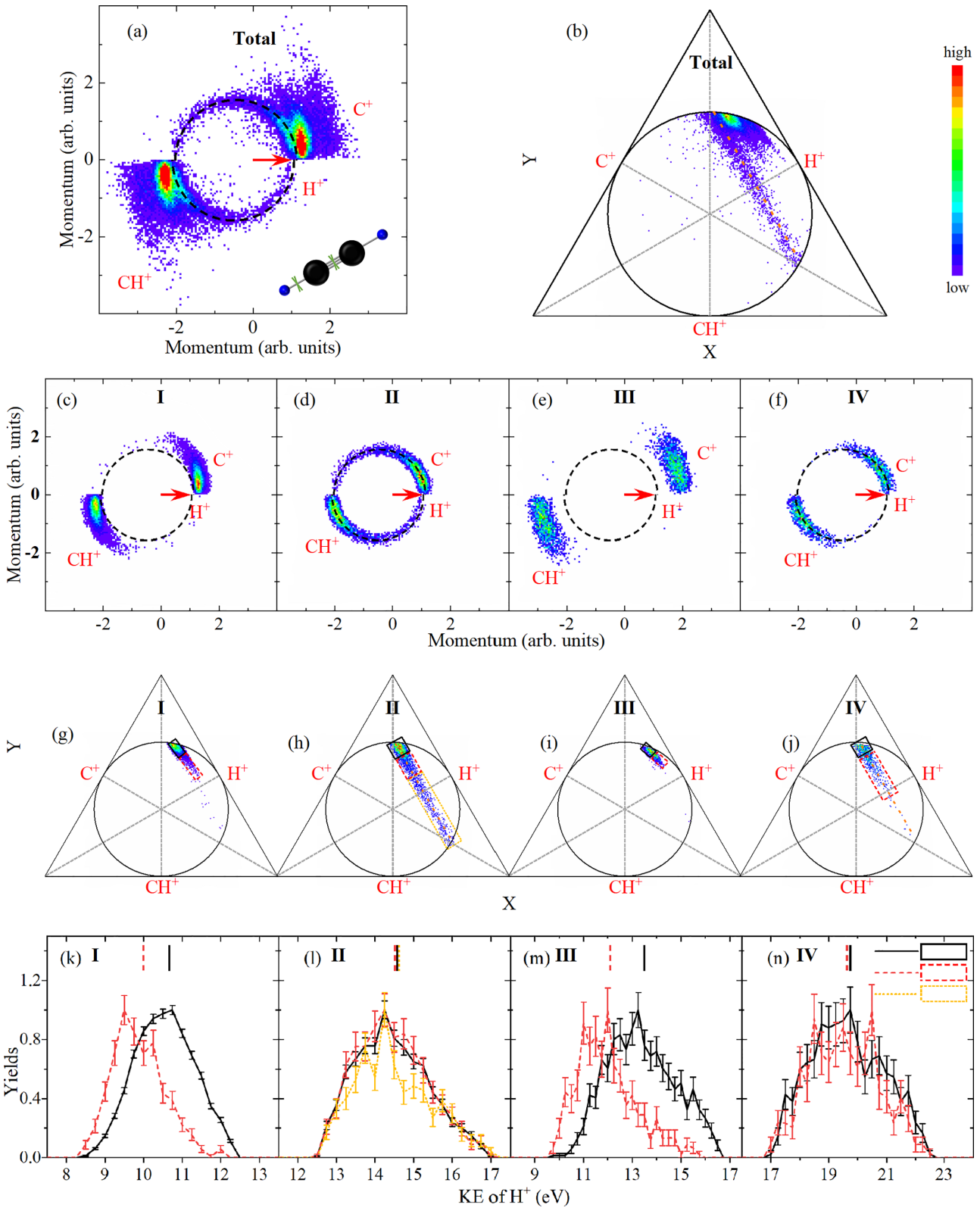

FIG. 2. (a) Newton diagram and (b) Dalitz plot with all the experimental data for the $H^+ + C^+ + CH^+$ channel. (c)–(f) Newton diagrams and (g)–(j) Dalitz plots with different KE filters I, II, III, and IV shown in Fig. 1, respectively. Black solid, red dashed, and orange dotted rectangles are different Dalitz filters used to deduce KE distributions shown in Figs. 2(k)–2(n). The orange dashed line in Figs. 2(b), 2(h), and 2(j) is parallel to the H^+ edge of the triangle. (k)–(n) KE distributions of H^+ with different Dalitz filters shown in (g)–(j), respectively. The color and style of the curves in (k)–(n) are the same as those of the corresponding Dalitz filters. Error bars of the data are calculated as the square root of the counts. The short vertical bar represents the mean KE values of H^+ for the curve with the same color and style.

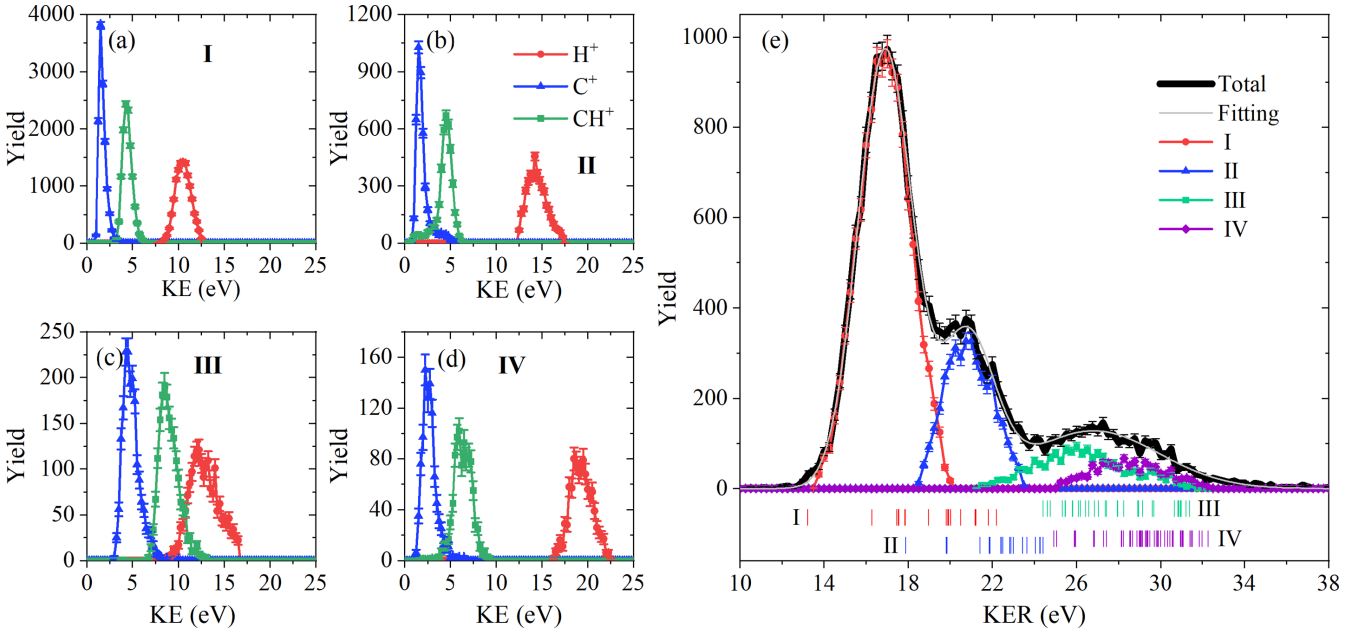

FIG. 3. (a)–(d) KE distributions of H^+ (red dot), C^+ (blue triangle), and CH^+ (green square) with filters of red ovals I–IV shown in Fig. 1(a), respectively. (e) The total KER distribution including all $H^+ + C^+ + CH^+$ events (thick black) and the partial plots decomposed by filters I (red dot), II (blue triangle), III (green square), and IV (purple rhomb). The gray curve presents Gaussian fitting of the total KER distribution. The calculated KER values from different electronic states are presented in the bottom of the figure.

the configuration from linear structure after more energy is deposited into the target.

The Newton diagram and the Dalitz plot for region IV are quite similar to region II. The strip parallel to the H^+ edge of the triangle, as well as the similar KE distributions of the proton for different filters, demonstrate that the emission of the proton is independent of the other two fragments. The fragmentation occurred through a similar sequential pathway to region II, i.e., a sequential pathway with the proton emitted in the first step, and then the intermediate C_2H^{2+} dissociates to C^+ and CH^+. Since the KER for region IV is much higher than region II, events in region IV are assigned to sequential fragmentation of higher excited electronic states of $C_2H_2{}^{3+}$.

Based on the above discussion, fragmentation mechanisms of the four isolated regions in the KE correlation spectra have been identified. The CH and CC bonds can break either simultaneously (regions I and III), or in a sequential manner with CH breaking in the first step followed by CC breaking (region II and IV). In Figs. 3(a)–3(d) we present the KE distributions for these different regions. Figure 3(e) displays the KER distribution for each region and the total KER distribution including all $H^+ + C^+ + CH^+$ events. By Gaussian fittings of the KER distribution cures for I to IV, the peak positions are determined to be 16.9, 20.8, 26.1, and 28.4 eV, respectively. These KER values are listed in Table I. The concerted fragmentation of low excited states contributes to region I with the lowest KER peaking at 16.9 eV. As the KER increases to 20.8 eV for region II, the sequential fragmentation channel becomes dominating. The increased KER from region I to region II is mainly from the KE of the proton, as can be seen by comparing Figs. 3(a) and 3(b). As the KER increases to 26.1 eV for region III, another concerted fragmentation channel makes the major contribution. This channel occurs in higher excited electronic states since the KER value is 9.2 eV higher than region I. By comparing the KE distributions between region III and region I, it seems that the exciting energy higher than the low-lying states distributes among all three fragments, since the KE of each fragment increases significantly from Fig. 3(a) to Fig. 3(c). When the KER increases further to 28.4 eV for region IV, sequential fragmentation with the proton emitted in the first step happened again. Both Figs. 3(b) and 3(d) show that the KE of

TABLE I. KER and branching ratios for regions I–IV, and counts and relative contribution of reaction channels T1I2 and T2I1 to these regions. The error for the relative ratio between T2I1 and T1I2 is obtained by consideration of the standard derivation of the counts for these two reaction channels. The error for the branching ratio is given by Gaussian fitting.

			Counts		Relative ratio
Region	KER (eV)	Branching ratio (%)	T1I2	T2I1	T2I1/T1I2 (%)
I	16.9	60.3 ± 0.3	11041	1071	9.7 ± 0.3
II	20.8	20.5 ± 0.8	3392	370	10.9 ± 0.6
III	26.1	12.8 ± 2.2	1562	195	12.5 ± 0.9
IV	28.4	6.4 ± 1.7	887	124	14.0 ± 1.3

TABLE II. Tentative assignments of the ground state and 165 excited states of $C_2H_2^{3+}$ responsible for the dissociation events in regions I–IV. The KER of the dissociated product, $H^+ + C^+(^2P_{1/2}) + CH^+(^1\Sigma_g^+)$, is computed at the CASSCF/cc-pVTZ level. The spin-orbit states of $C^+(^4P_{1/2})$ and $C^+(^2D_{5/2})$ are 5.33 and 9.29 eV above the ground state $C^+(^2P_{1/2})$, respectively, taken from the NIST atomic spectra database [46]. The excited states of $CH^+(^3\Pi_u)$ and $CH^+(^1\Pi_u)$ are 1.33 and 3.27 eV higher than the ground state of $CH^+(^1\Sigma_g^+)$ at the CASSCF/cc-pVTZ level, respectively.

Description	Number of states	Assignment	KER range (eV)	
			Theory	Experiment
Ground state	1	Onset	13.2	12.8
σ(C-C) ($5a_1$) to π or π^*	19	I	13.2–22.2	13–20
σ(C-H) ($4a_1$) to higher orbitals	22	II	17.9–24.4	18–24
σ(C-C) ($5a_1$) to σ^*(C-C) ($6a_1$)	45	III	24.4–31.4	21–32
Primarily weakened σ(C-H) ($3a_1$ or $4a_1$)	79	IV	24.9–32.3	25–32

the proton is much higher than the other two fragments, since in these regions the proton is emitted in the first step of the sequential process, and experiences Coulomb repulsion of the doubly charged C_2H^{2+}.

B. Electronic states contributing to different pathways

The electronic ground state of $C_2H_2^{3+}(^2\Pi_u)$ has an unpaired electron occupying one of the π_u bonding orbitals and the respective C-C and C-H bond lengths are 1.576 and 1.286 Å. Assuming the $C_2H_2^{3+}$ lies along the z axis and belongs to the C_{2v} point group, the dominant electronic configuration is $(3a_1)^2(4a_1)^2(5a_1)^2(1b_1)^1(1b_2)^0$ or $(3a_1)^2(4a_1)^2(5a_1)^2(1b_1)^0(1b_2)^1$. Here $3a_1$ and $4a_1$ correspond to two occupied σ(C-H) bond orbitals, $5a_1$ is the occupied σ(C-C) orbital made up of $2p_z$(C), while the $1b_1$ and $1b_2$ are a pair of degenerate π_x and π_y orbitals in the CC triple bond. The optimized $C_2H_2^{3+}(^2\Pi_u)$ structure is 13.2 eV above the potential energy of $H^+ + C^+(^2P_{1/2}) + CH^+(^1\Sigma_g^+)$. Supposing the $C_2H_2^{3+}(^2\Pi_u)$ dissociates promptly into $H^+ + C^+(^2P_{1/2}) + CH^+(^1\Sigma_g^+)$, the sum translational energies of the three fragments, i.e., KER, should be 13.2 eV. This is consistent with the onset of the total KER distribution for all $H^+ + C^+ + CH^+$ events observed in Fig. 3(e). However, a large body dissociation event is found to have a KER larger than 13.2 eV, indicating that the major contributions are from excited electronic states of $C_2H_2^{3+}$, rather than the ground state.

Based on the optimized $C_2H_2^{3+}(^2\Pi_u)$ structure, the vertical excited energies of $C_2H_2^{3+}$ in the energy range from 13.2 to 32.3 eV [relative to the energy of dissociated ions of $H^+ + C^+(^2P_{1/2}) + CH^+(^1\Sigma_g^+)$] are computed at the CASSCF level. We were unable to obtain a stable structure for the excited $C_2H_2^{3+}$ ion. The $1\ ^2A_1$, $1\ ^2A_2$, $1\ ^4A_1$, $1\ ^4B_1$, $1\ ^4B_2$, $1\ ^4A_2$, $1\ ^6A_1$, $1\ ^6B_1$, $1\ ^6B_2$, $1\ ^6A_2$ states (see the dominant configuration shown in the Supplemental Material [43]) are all repulsive. Presumably all the excited states are repulsive. For the excited-state calculations, the state-averaging included the contributions of the ground state and 165 excited states of $C_2H_2^{3+}$, including 86 doublet, 64 quartet, and 15 sextet states. These states are sorted into four groups as summarized in Table II. Details of these states are listed in Tables S1–S4 in the Supplemental Material [43]. These calculated KER values for different electronic states are represented at the bottom of Fig. 3(e). The calculated KER values fit well with the measured KER distribution.

The 19 excited states in Table S1 in the Supplemental Material [43] are mostly formed by promoting an electron from σ(C-C) orbital ($5a_1$) to higher π or π^* orbitals. Given the repulsive nature and the disturbed σ(C-C) orbital, these states are expected to dissociate into $H^+ + C^+(^2P_{1/2}) + CH^+(^1\Sigma_g^+)$ ions concertedly, and contribute to the $H^+ + C^+ + CH^+$ events with KER ranging from 13.2 to 22.2 eV. This remarkably agrees with the KER distribution for region I [red curve with dots in Fig. 3(e)]. The slightly higher KER range given by our theoretical predictions than the experimental values may be due to (i) the energy partition from transitional motions of $CH^+(^1\Sigma_g^+)$ ions into rotational and/or vibrational degrees of freedom during the dissociation process and (ii) the fact that the vertical excitation energy is used here to determine the KER for $H^+ + C^+(^2P_{1/2}) + CH^+(^1\Sigma_g^+)$ dissociation.

The concerted fragmentation events in region III are likely contributed by over 45 excited states shown in Table S3 in the Supplemental Material [43]. Most states listed in this table involve electronic excitations from σ(C-C) orbital ($5a_1$) to σ^*(C-C) orbital ($6a_1$) or/and π or π^* orbitals. Given the repulsive nature of these excited states and the intact σ(C-H) bonding orbitals, the dissociations into three ions should occur concertedly, yielding the $H^+ + C^+ + CH^+$ events with KER from 24.4 to 31.4 eV. This consistently matches with the range of KER distribution for region III [green curve with squares in Fig. 3(e)].

The sequential dissociation events with C-H bond breaking in the first step are assigned to excited states with a weakened C-H bond. We have identified 22 (Table S2 in the Supplemental Material [43]) and 79 (Table S4 in the Supplemental Material) excited states responsible for the dissociation events in regions II and IV, respectively. In Table S2 in the Supplemental Material, the σ(C-H) bond in the excited states is weakened because of the electronic excitation out of the σ(C-H) orbital ($4a_1$) to other higher orbitals. As the σ(C-H) bond is depleted of electron(s) and gets weakened, the $C_2H_2^{3+}$ ions are expected first to undergo $[H\text{-}CCH]^{3+}$ bond cleavage and give $H^+ + CCH^{2+}$ (step 1), and then the ethynyl di-cation cleaves its CC bond, $CCH^{2+} \rightarrow C^+ + CH^+$ (step 2). The theoretical KER of the contributed 22 excited states falls between 17.9 and 24.4 eV relative to the $H^+ + C^+(^2P_{1/2}) +$

$CH^+(^1\Sigma_g{}^+)$. This is consistent with KER distribution of region II displayed by the blue curve with triangles in Fig. 3(e). Likewise, a higher set (79) of excited states which primarily have weakened σ(C-H) orbitals ($3a_1$ or $4a_1$) is responsible for the sequential C-H and C-C bond breaking events and contributes to $H^+ + C^+ + CH^+$ events with KER from 24.9 to 32.3 eV. This agrees with the KER distribution of region IV displayed by the purple curve with rhombs in Fig. 3(e).

C. Branching ratios of different pathways

Finally we consider the branching ratios of different mechanisms associating to regions I to IV in the KE correlation spectra, and the influence of reaction channels, namely, T1I2 and T2I1, to these mechanisms. To get the branching ratios of the four structures, a Gaussian fitting of the total KER distribution is performed with the peak centers listed in Table I. As displayed in this table, the branching ratios for region I, II, III, and IV are 60.3, 20.5, 12.8, and 6.4%, respectively. Concerted fragmentation following the excitation of one electron from the σ(C-C) orbital ($5a_1$) to a higher orbital (region I) is the major contribution to the $H^+ + C^+ + CH^+$ channel. As KER is increased, the branching ratio of associated mechanisms decreases. Such a trend can be explained as that excitation of electrons to higher orbitals usually corresponds to stronger projectile-target interaction and a smaller impact parameter, and thus leads to smaller reaction cross sections. The relative contributions arising from two different charge exchanging and ionization channels, T1I2 and T2I1, are also listed in Table I. It can be seen that the T1I2 reaction channel is the major contribution to all four regions, while T2I1 makes a minor contribution. Nevertheless, as the KER increases from I to IV, the ratio between contributions of T2I1 and T1I2 increases gradually. The T2I1 reaction is more efficient to initiate fragmentation mechanisms that lead to higher KER, demonstrating that the fragmentation mechanisms can be influenced by collision dynamics between the projectile and the target. This is probably due to the fact that the proportions of enrolled electronic states are not the same for different charge exchange reactions. The projectile-target interaction is stronger for the T2I1 channel compared to the T1I2 channel, and thus T2I1 is more efficient for population of higher excited electronic states listed in Tables S3 and S4 in the Supplemental Material [43].

IV. CONCLUSION

Fragmentation dynamics of $C_2H_2{}^{3+} \rightarrow H^+ + C^+ + CH^+$ is investigated by 50-keV/u Ne^{8+} impact employing a reaction microscope. The H^+, C^+, and CH^+ are recorded in coincidence with the scattered projectile of either Ne^{7+} (T1I2) or Ne^{6+} (T2I1). Momentum vectors of all three fragments are obtained with which detailed analysis of the momentum and KE correlation are available. Four separated structures I to IV with KER peaking at 16.9, 20.8, 26.1, and 28.4 eV are observed in the energy correlation spectra. By analyzing the Newton diagram and the Dalitz plot, fragmentation mechanisms associated to these structures are clearly identified. The structures with KER peaking at 16.9 and 26.1 eV are assigned to concerted fragmentation of $C_2H_2{}^{3+}$ with one electron excited from σ(C-C) ($5a_1$) to higher orbitals. Also, the sequential fragmentation process with CH cleavage in the first step followed by CC cleavage is identified. These sequential processes lead to KERs peaking at 20.8 and 28.4 eV, and are assigned to excited states with weakened C-H bond during ionization. In addition, we found that the reaction channel T1I2 accounts for the majority of the $H^+ + C^+ + CH^+$ events in all four structures, while the T2I1 reaction only makes a minor contribution. It is interesting that the proportion of T2I1 in structures I to IV increases as the KER increases, demonstrating that the dynamics of charge exchange between the projectile and the target can influence fragmentation mechanisms.

ACKNOWLEDGMENTS

The work was jointly supported by the National Key Research and Development Program of China under Grant No. 2017YFA0402300 and the National Natural Science Foundation of China under Grant No. 12274416. The authors acknowledge the 320-kV platform staff at Institute of Modern Physics, Chinese Academy of Sciences for their technical support. The authors would like to thank for the supports from national laboratory of Heavy Ion Research Facility in Lanzhou (HIRFL).

[1] A. G. G. M. Tielens, Rev. Mod. Phys. **85**, 1021 (2013).
[2] S. Lehnert, *Biomolecular Action of Ionizing Radiation* (CRC Press, Boca Raton, FL, 2007).
[3] D. Reiter and R. K. Janev, Contrib. Plasma Phys. **50**, 986 (2010).
[4] S. Hsieh and J. H. D. Eland, J. Phys. B: At. Mol. Opt. Phys. **30**, 4515 (1997).
[5] N. Neumann, D. Hant, L. P. H. Schmidt, J. Titze, T. Jahnke, A. Czasch, M. S. Schöffler, K. Kreidi, O. Jagutzki, H. Schmidt-Böcking, and R. Dörner, Phys. Rev. Lett. **104**, 103201 (2010).
[6] C. Wu, C. Wu, D. Song, H. Su, Y. Yang, Z. Wu, X. Liu, H. Liu, M. Li, Y. Deng, Y. Liu, L.-Y. Peng, H. Jiang, and Q. Gong, Phys. Rev. Lett. **110**, 103601 (2013).
[7] A. Khan, L. C. Tribedi, and D. Misra, Phys. Rev. A **92**, 030701(R) (2015).
[8] E. Wang, X. Shan, Z. Shen, M. Gong, Y. Tang, Y. Pan, K.-C. Lau, and X. Chen, Phys. Rev. A **91**, 052711 (2015).
[9] S. Yan, X. L. Zhu, P. Zhang, X. Ma, W. T. Feng, Y. Gao, S. Xu, Q. S. Zhao, S. F. Zhang, D. L. Guo, D. M. Zhao, R. T. Zhang, Z. K. Huang, H. B. Wang, and X. J. Zhang, Phys. Rev. A **94**, 032708 (2016).
[10] H. J. Yang, E. Wang, W. X. Dong, M. Gong, Z. Shen, Y. Tang, X. Shan, and X. Chen, Phys. Rev. A **97**, 052703 (2018).
[11] J. Eland, Mol. Phys. **61**, 725 (1987).
[12] M. R. Jana, B. Ray, P. N. Ghosh, and C. P. Safvan, J. Phys. B: At. Mol. Opt. Phys. **43**, 215207 (2010).
[13] K. Saha, S. Banerjee, and B. Bapat, Chem. Phys. Lett. **607**, 85 (2014).
[14] Z. Shen, E. Wang, M. Gong, X. Shan, and X. Chen, J. Chem. Phys. **145**, 234303 (2016).

[15] J. Rajput, T. Severt, B. Berry, B. Jochim, P. Feizollah, B. Kaderiya, M. Zohrabi, U. Ablikim, F. Ziaee, K. Raju P., D. Rolles, A. Rudenko, K. D. Carnes, B. D. Esry, and I. Ben-Itzhak, Phys. Rev. Lett. **120**, 103001 (2018).
[16] H. Kumar, P. Bhatt, C. P. Safvan, and J. Rajput, J. Chem. Phys. **148**, 064302 (2018).
[17] A. Hishikawa, H. Hasegawa, and K. Yamanouchi, Chem. Phys. Lett. **361**, 245 (2002).
[18] R. Guillemin, P. Decleva, M. Stener, C. Bomme, T. Marin, L. Journel, T. Marchenko, R. K. Kushawaha, K. Jänkälä, N. Trcera, K. P. Bowen, D. W. Lindle, M. N. Piancastelli, and M. Simon, Nat. Commun. **6**, 6166 (2015).
[19] P. Bhatt, R. Singh, N. Yadav, and R. Shanker, Phys. Rev. A **86**, 052708 (2012).
[20] A. Khan, L. C. Tribedi, and D. Misra, Phys. Rev. A **96**, 012703 (2017).
[21] R. Singh, P. Bhatt, N. Yadav, and R. Shanker, J. Phys. B: At. Mol. Opt. Phys. **46**, 085203 (2013).
[22] T. Jahnke, R. Guillemin, L. Inhester, S.-K. Son, G. Kastirke, M. Ilchen, J. Rist, D. Trabert, N. Melzer, N. Anders, T. Mazza, R. Boll, A. De Fanis, V. Music, T. Weber, M. Weller, S. Eckart, K. Fehre, S. Grundmann, A. Hartung *et al.*, Phys. Rev. X **11**, 041044 (2021).
[23] A. Hishikawa, A. Matsuda, M. Fushitani, and E. J. Takahashi, Phys. Rev. Lett. **99**, 258302 (2007).
[24] Y. H. Jiang, A. Rudenko, O. Herrwerth, L. Foucar, M. Kurka, K. U. Kühnel, M. Lezius, M. F. Kling, J. van Tilborg, A. Belkacem, K. Ueda, S. Düsterer, R. Treusch, C. D. Schröter, R. Moshammer, and J. Ullrich, Phys. Rev. Lett. **105**, 263002 (2010).
[25] H. Ibrahim, B. Wales, S. Beaulieu, B. E. Schmidt, N. Thiré, E. P. Fowe, É. Bisson, C. T. Hebeisen, V. Wanie, M. Giguére, J.-C. Kieffer, M. Spanner, A. D. Bandrauk, J. Sanderson, M. S. Schuurman, and F. Légaré, Nat. Commun. **5**, 4422 (2014).
[26] X. Gong, Q. Song, Q. Ji, K. Lin, H. Pan, J. Ding, H. Zeng, and J. Wu, Phys. Rev. Lett. **114**, 163001 (2015).
[27] C. E. Liekhus-Schmaltz, I. Tenney, T. Osipov, A. Sanchez-Gonzalez, N. Berrah, R. Boll, C. Bomme, C. Bostedt, J. D. Bozek, S. Carron, R. Coffee, J. Devin, B. Erk, K. R. Ferguson, R. W. Field, L. Foucar, L. J. Frasinski, J. M. Glownia, M. Gühr, A. Kamalov *et al.*, Nat. Commun. **6**, 8199 (2015).
[28] C. Burger, N. G. Kling, R. Siemering, A. S. Alnaser, B. Bergues, A. M. Azzeer, R. Moshammer, R. de Vivie-Riedle, M. Kübel, and M. F. Kling, Faraday Discuss. **194**, 495 (2016).
[29] S. Xu, H. Zhao, X. Zhu, D. Guo, W. Feng, K.-C. Lau, and X. Ma, Phys. Chem. Chem. Phys. **20**, 27725 (2018).
[30] B. Jochim, B. Berry, T. Severt, P. Feizollah, M. Zohrabi, K. R. P., E. Wells, K. D. Carnes, and I. Ben-Itzhak, J. Phys. Chem. Lett. **10**, 2320 (2019).
[31] Y. Wang, X. Shi, J. Zhou, S. Xu, D. Guo, S. Yan, X. Zhu, and X. Ma, Phys. Rev. A **101**, 042706 (2020).
[32] T. Mizuno, T. Yamada, H. Tsuchida, Y. Nakai, and A. Itoh, J. Phys.: Conf. Ser. **163**, 012039 (2009).
[33] S. De, J. Rajput, A. Roy, P. N. Ghosh, and C. P. Safvan, Phys. Rev. A **77**, 022708 (2008).
[34] S. Yoshida, T. Majima, T. Asai, M. Matsubara, H. Tsuchida, M. Saito, and A. Itoh, Nucl. Instrum. Methods Phys. Res. Sect. B **408**, 203 (2017).
[35] S. Xu, X. L. Zhu, W. T. Feng, D. L. Guo, Q. Zhao, S. Yan, P. Zhang, D. M. Zhao, Y. Gao, S. F. Zhang, J. Yang, and X. Ma, Phys. Rev. A **97**, 062701 (2018).
[36] T. Jiang, B. Wang, Y. Zhang, L. Wei, S. Chen, W. Yu, Y. Zou, L. Chen, and B. Wei, Phys. Rev. A **100**, 022705 (2019).
[37] R. Dörner, V. Mergel, O. Jagutzki, L. Spielberger, J. Ullrich, R. Moshammer, and H. Schmidt-Böcking, Phys. Rep. **330**, 95 (2000).
[38] J. Ullrich, R. Moshammer, A. Dorn, R. Dörner, L. P. H. Schmidt, and H. Schmidt-Böcking, Rep. Prog. Phys. **66**, 1463 (2003).
[39] X. Ma, R. T. Zhang, S. F. Zhang, X. L. Zhu, W. T. Feng, D. L. Guo, B. Li, H. P. Liu, C. Y. Li, J. G. Wang, S. C. Yan, P. J. Zhang, and Q. Wang, Phys. Rev. A **83**, 052707 (2011).
[40] R. Dalitz, London Edinburgh Dublin Philos. Mag. J. Sci. **44**, 1068 (1953).
[41] H. Werner and P. J. Knowles, J. Chem. Phys. **82**, 5053 (1985).
[42] P. J. Knowles and H.-J. Werner, Chem. Phys. Lett. **115**, 259 (1985).
[43] See Supplemental Material at http://link.aps.org/supplemental/10.1103/PhysRevA.107.012811 for more details on dominant electron configurations contributing to different fragmentation mechanisms.
[44] H.-J. Werner, P. J. Knowles, G. Knizia, F. R. Manby, M. Schütz *et al.*, MOLPRO, version 2022.2, a package of ab initio programs, http://www.molpro.net.
[45] B. Ren, Z. Xia, Y. Zhang, L. Wei, W. Yu, J. Han, B. Wang, Y. Zou, L. Chen, and B. Wei, Phys. Rev. A **104**, 022811 (2021).
[46] A. Kramida, Yu. Ralchenko, J. Reader, and NIST ASD Team, NIST Atomic Spectra Database, 2021, https://doi.org/10.18434/T4W30F.